# The Rayleigh–Taylor instability of a viscous liquid layer resting on a plane wall

By LORI A. NEWHOUSE AND C. POZRIKIDIS

Department of Applied Mechanics and Engineering Sciences, R-011, University of California, San Diego, La Jolla, CA 92093, USA

The nonlinear Rayleigh–Taylor instability of a liquid layer resting on a plane wall below a second liquid of higher density is considered. Under the assumption of creeping flow, the motion is studied as a function of surface tension and the ratio of the viscosities of the two fluids. The flow induced by the deformation of the layer is represented by an interfacial distribution of Green's functions. A Fredholm integral equation of the second kind is derived for the density of the distribution, and is solved by successive iteration. The results show that for small and moderate surface tension, the instability of the layer leads to the formation of a periodic array of viscous plumes which penetrate into the overlying fluid. The morphology of these plumes strongly depends upon the viscosity ratio and surface tension. When the viscosity of the overlying fluid is comparable with or larger than that of the layer, the plumes are composed of a well-defined leading drop on top of a narrow stem. When the viscosity of the overlying fluid is smaller than that of the layer, the plumes take the form of a compact column of rising fluid. The size of the drop leading a plume is roughly proportional to the initial thickness of the layer. When surface tension is sufficiently small, ambient fluid is entrained into the leading drop and circulates in a spiral pattern. Convection currents generated by the rising plumes are visualized with streamline patterns, and the rate of thinning of the remnant layer, as well as the speed of the rising drop or plumes, are discussed.

## 1. Introduction

Liquid layers resting on solid surfaces are frequently encountered in nature and industry. In coating processes, for instance, gelatin emulsions and magnetic suspensions are coated on solid supports to produce photographic films and magnetic disks. Thin layers of suspending fluid develop at the late stages of coalescence of bubbles, drops, and solid particles. Similarly, thin layers of liquid develop around the grains and fibres during the flow of immiscible liquids through underground porous media and industrial filters. Thin aqueous layers of biological fluids constitute integral parts of many organs; a characteristic example is the thin film wetting the surface of the eye. Finally, layers of viscous fluids arise in several geophysical applications; examples are layers of hot mantle material surrounding the Earth's core, and sinking slabs of tectonic plates.

There is considerable current interest in studying the dynamics of liquid layers from both an industrial and a fundamental perspective. From the industrial viewpoint, understanding and controlling the deformation of viscous layers provides useful guidelines for eliminating the onset of hydrodynamic instabilities. These instabilities may be responsible for coating non-uniformities that lead to streaked

and mottled surfaces and degrade the quality of the end product. Furthermore, describing the detailed, thin dynamics of liquid layers is requisite for understanding the physics of composite processes involving the coalescence of solid and flexible particles; characteristic examples are flotation and filtration. On an academic level, the study of layer dynamics falls into a more general category of problems concerned with the evolution of passive and active interfaces. Issues of interest are the formation of ordered interfacial structures and the long-time, asymptotic behaviour of the deformed interfaces. From a geophysical perspective, analysing the fluid motion induced by the instability of liquid layers provides rational models for predicting continental drift and volcanic activity.

In general, a liquid layer may deform owing to an external flow or to an external body force. In both cases, small inherent non-uniformities are spontaneously amplified. Of the instabilities due to a body force, the one most commonly encountered is the gravitational instability – the Rayleigh–Taylor instability (Rayleigh 1990) – and its study has become a classical topic in fluid mechanics. In its classical interpretation, the Rayleigh–Taylor instability is the instability of the interface between two superposed fluids of different densities where the heavier fluid lies on top. From a more general perspective, it may be defined as the instability of an accelerated fluid interface where the inertial force associated with the acceleration is directed from the heavy to the light fluid.

Early work on the Rayleigh–Taylor instability consisted of linear stability analyses whose main objectives were to define the conditions for instability and to determine the most unstable mode as a function of the physical properties of the fluids (Chandrasekhar 1961, p. 428; Menikoff *et al.* 1977, 1978). To describe the morphology, evolution, and nonlinear interactions between emerging structures, weakly and highly nonlinear theories have also been developed. These may be classified into two basic categories depending on the Reynolds number that prevails during the flow. The majority of previous nonlinear studies are based on the assumption of potential flow, and apply for semi-infinite fluids (Sharp 1984; Baker *et al.* 1987; Gardner *et al.* 1988; Jacobs & Catton 1988*a*, *b*; Kerr 1988; Tryggvason 1988; Zufiria 1988). The approximation of potential, inviscid flow is acceptable as long as the timescale of the instability is much shorter than the timescale of vorticity diffusion; in this manner, viscous effects are confined to thin layers along the fluid interface.

The second category of nonlinear theories includes studies of the instability under conditions of creeping motion. These pertain to configurations composed of single or multiple liquid layers resting on a plane wall. Babchin *et al.* (1983) presented a formulation in the context of lubrication theory (valid for long waves) and argued that the presence of an ambient shear flow suppresses the nonlinear growth and leads to saturation. Yiantsios & Higgins (1989) extended this theory to account for the presence of an overlying fluid, and performed numerical calculations (based on the boundary-integral method) to describe the well-advanced stages of evolution. Their work will be discussed further in our paper. A number of authors addressed stable layer configurations with emphasis on the rate of dampening of external perturbations (Orchard 1963; Keunings & Bousfield 1987). With the exception of the analysis of Yiantsios & Higgins (1989), all previous nonlinear analyses were performed under the premises of lubrication theory. This theory is valid only when surface tension is sufficiently large, so that the growth of perturbations of small and moderate wavelengths is suppressed. A second assumption of all previous viscous nonlinear analyses is that the viscosity of the overlying fluid is of the same order or

lower order than that of the liquid layer. When this assumption cannot be made, the motion of the overlying fluid must be taken into consideration, leading to a rather complex mathematical problem. Further work relaxing the above two assumptions is needed in order to determine the behaviour under general conditions.

Considering the Rayleigh–Taylor instability from a physical viewpoint, it is instructive to compare the purely inviscid with the purely viscous evolution. In the inviscid case, the evolution depends on the wavelength of the perturbation and on the ratio of the densities of the two fluids (Tryggvason 1988). It is well established that for small density ratios the interface rolls up into spiral vortices, a consequence of the onset of secondary instabilities of the Kelvin–Helmholtz type. For large density ratios, the heavy fluid penetrates the light fluid through the development of spikes, leaving behind compact rising drops of light fluid. In the purely viscous case, the density ratio serves only to define the rate of the motion and is of no dynamical significance. Here, the viscosity ratio between the two fluids, $\lambda$, is of primary dynamical concern. There is evidence in the literature that $\lambda$ plays a critical role by prohibiting certain types of interfacial motions or introducing new types of motion. This is suggested particularly by the linear analysis of Hooper & Boyd (1983), by the experiments of Olson & Singer (1985), and by the numerical calculations of Pozrikidis (1990*a*). Further work is required to delineate the exact effect of $\lambda$ and to bridge the parametric gap between the purely inviscid and the purely viscous motion.

In this paper, we study the nonlinear, viscous instability of a liquid layer resting on a plane solid wall below a second liquid of higher density and arbitrary viscosity. We confine our attention to conditions of creeping flow and to cases of two-dimensional motion. Our analysis is valid for interfacial perturbations of any wavelength (no assumption regarding the magnitude of surface tension is made) and for fluids of arbitrary viscosity. Our objective is to present a coherent parametric investigation delineating the effects of viscosity ratio, surface tension, and layer thickness. We are particularly interested in describing the highly nonlinear, well-advanced stages of the instability, extending previous linearized and asymptotic theories. We pay attention to the fluid motion induced by the layer evolution and to the nonlinear growth of the developed structures. Our analysis entails parametric investigations in which we impose an initial periodic two-dimensional perturbation and compute the subsequent layer evolution.

Our study is based on the numerical solution of the equations of creeping motion within both the liquid layer and the overlying fluid. To describe the evolution of the interface in a computationally efficient manner, we develop a boundary-integral representation expressing the flow in terms of a distribution of Green's functions over the fluid interface. These Green's functions are periodic in a direction parallel to the wall and yield zero velocity along the wall. Eventually, we reduce the problem to solving a Fredholm integral equation of the second kind for the density of the Green's functions. After proving the uniqueness of solution and the convergence of the Neumann series of the derived equation, we develop a numerical method of solution which is based on successive iteration.

In §2 we formulate the problem, review the results of linear stability analysis, develop the boundary-integral representation, and formulate the problem as an integral equation. In §3 we present and discuss results of our computations. We conclude in §4 with closing remarks.

## 2. Problem formulation

We consider the evolution of a liquid layer of thickness $b$ resting on a plane solid surface below a second liquid of higher density (figure 1). We label the layer with the subscript 1 and the overlying semi-infinite fluid with the subscript 2. The interface is characterized by constant surface tension $\gamma$. We confine our attention to cases where the Reynolds number of the flow remains negligible throughout the evolution. The flow within the layer and the overlying fluid is governed by Stokes' equation with the gravity term included:

$$-\nabla P + \mu_\alpha \nabla^2 \boldsymbol{u} + \rho_\alpha \boldsymbol{g} = 0 \qquad (2.1)$$

where $\alpha = 1, 2$. We require the velocity to vanish along the solid wall, and the velocity and tangential component of the surface stress to be continuous across the fluid interface. We allow a discontinuity in the normal component of the surface stress at the interface, but require that it is compensated by surface tension. The problem is to describe the evolution of the layer from a given initial configuration.

### 2.1. *Linear stability theory*

A number of authors have carried out the classical linear stability analysis of the configuration shown in figure 1, assuming infinitesimal interfacial perturbations (see for instance Jain & Ruckenstein 1976). Because the basic state is independent of direction in a plane parallel to the wall, it suffices to consider two-dimensional perturbations periodic in the $x$-direction. Linear stability theory provides the growth rate $\sigma$ of a sinusoidal perturbation with wavelength $l$ as a function of the viscosity ratio $\lambda = \mu_1/\mu_1$, the surface-tension group $S = \gamma k^2/\Delta\rho g$, and the wavenumber or reduced layer thickness $\beta = kb$; $k$ is the wavenumber, $k = 2\pi/l$, and $\Delta\rho = \rho_2 - \rho_1 > 0$. Positive $\sigma$ implies instability, whereas negative $\sigma$ implies stability. The result is

$$\hat{\sigma} \equiv \frac{\sigma k \mu_1}{\Delta\rho g} = \tfrac{1}{2}(1 - S)\, G(\beta, \lambda), \qquad (2.2)$$

where the function $G$ is defined as

$$G(\beta, \lambda) = \frac{\tfrac{1}{2}\sinh 2\beta - \beta + \lambda[\sinh^2\beta - \beta^2]}{(1 - \lambda^2)\,\beta^2 + [\cosh\beta + \lambda\sinh\beta]^2} \qquad (2.3)$$

and may be shown to be positive definite. In the special case of fluids with the same viscosity, $\lambda = 1$, equation (2.2) simplifies to

$$\hat{\sigma} = \tfrac{1}{4}(1 - S)\{1 - e^{-2\beta}(1 + 2\beta + 2\beta^2)\}. \qquad (2.4)$$

There are two ways to interpret the above results. First, we may keep the wavenumber $k$ constant and vary the film thickness $b$. We then find that the layer is stable when $S < 1$ and unstable when $S > 1$, independent of $\lambda$. Physically, this implies that the instability of the layer is determined solely by a balance between gravitational and capillary forces. A more natural interpretation arises by maintaining $b$ constant and varying the wavenumber $k$. To elaborate on this, we recast (2.2) in the equivalent form

$$\tilde{\sigma} \equiv \frac{\sigma \mu_1}{\Delta\rho g b} = \frac{1}{2}\frac{(1 - \Gamma\beta^2)}{\beta}\, G(\beta, \lambda), \qquad (2.5)$$

where $\Gamma$ is the inverse Bond number $\Gamma = \gamma/\Delta\rho g b^2$. The layer is unstable when
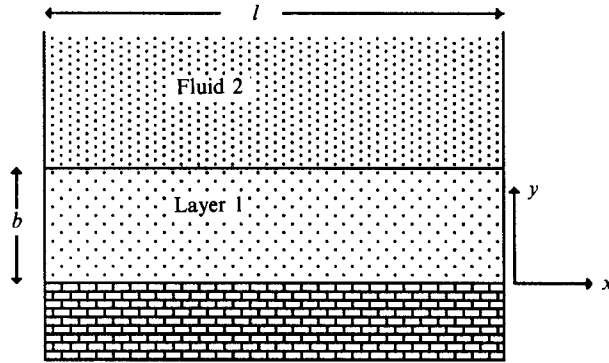
FIGURE 1. A liquid layer resting on a plane wall below a second semi-infinite fluid; $l$ is the wavelength of a periodic perturbation.
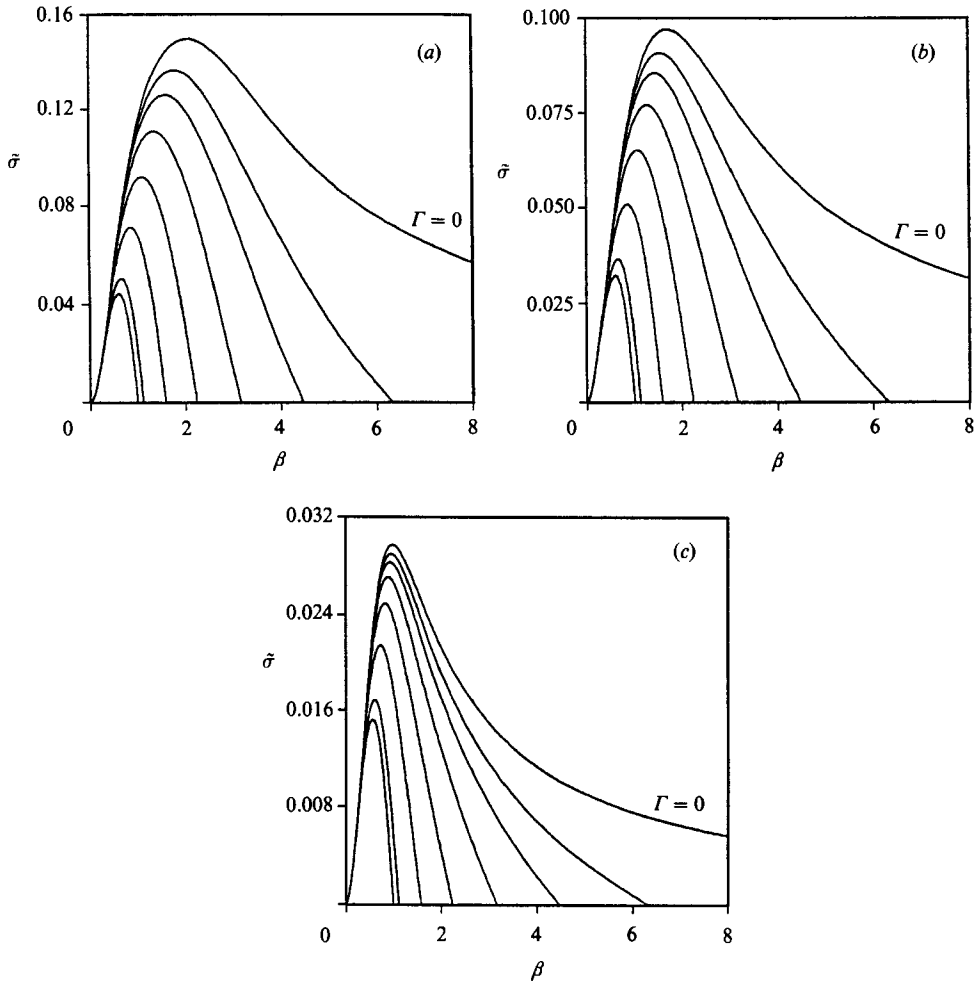


FIGURE 2. Growth rate predicted by linear theory $\tilde{\sigma}$ as a function of wavenumber $\beta$ for inverse Bond number $\Gamma = 0$, 0.025, 0.05, 0.1, 0.2, 0.4, 0.8, 1.0: (a) $\lambda = 0.1$, (b) $\lambda = 1.0$, (c) $\lambda = 10.0$.

$\beta < \Gamma^{-\frac{1}{2}}$, that is for small wavenumbers or large wavelengths, and is stable otherwise. In the absence of surface tension, $\Gamma = 0$, all wavelengths are unstable. This behaviour is independent of $\lambda$, a consequence of the absence of flow in the unperturbed state. In figure 2(*a–c*) we present three plots of the growth rate $\tilde{\sigma}$ as a function of the reduced wavenumber $\beta$ for three values of $\lambda$ ($\lambda = 0.1$, 1.0, and 10.0) and for several values of $\Gamma$. We note that not only the wavenumber for incipient stability, but also the general behaviour of the growth curves, is insensitive to $\lambda$. Increasing the inverse Bond number, that is increasing $\gamma$ or decreasing $\Delta\rho$, shifts the wavenumber corresponding to the maximum growth rate to lower values, favouring the growth of longer waves. Increasing the viscosity of the upper fluid, that is increasing $\lambda$, substantially reduces the growth rate of the perturbation.

### 2.2. *Formulation as an integral equation*

In this section we develop a boundary-integral representation capable of describing large, two-dimensional layer deformations. Before proceeding with this representation, it is necessary to introduce the periodic Green's function for Stokes flow in a two-dimensional domain bounded by a solid plane wall. Physically, this Green's function represents the flow produced by an infinite $x$-periodic array of point forces of separation $l$ placed above the wall. The corresponding velocity, pressure, and stress are given in terms of the three tensors $\boldsymbol{G}$, $\boldsymbol{p}$, and $\boldsymbol{T}$ as

$$u_i(\boldsymbol{x}) = G_{ij}(\boldsymbol{x}, \boldsymbol{x}_0)\, a_j, \tag{2.6a}$$

$$P(\boldsymbol{x}) = \mu p_j(\boldsymbol{x}, \boldsymbol{x}_0)\, a_j, \tag{2.6b}$$

$$\sigma_{ik}(\boldsymbol{x}) = \mu T_{ijk}(\boldsymbol{x}, \boldsymbol{x}_0)\, a_j, \tag{2.6c}$$

where the strength of each point force is $4\pi\boldsymbol{a}$, and one of the point forces is placed at the point $\boldsymbol{x}_0$. The tensor $\boldsymbol{G}$ satisfies the following conditions: it is periodic in the $x$-direction, that is $G_{ij}(x, y, \boldsymbol{x}_0) = G_{ij}(x+l, y, \boldsymbol{x}_0)$; it vanishes when $\boldsymbol{x}$ lies on the wall at $y = w$, that is $G_{ij}(x, y = w, \boldsymbol{x}_0) = 0$; and, as $\boldsymbol{x} \to \boldsymbol{x}_0$, it reduces to the free-space two-dimensional Stokeslet $\boldsymbol{S}$,

$$S_{ij} = -\delta_{ij} \ln|\hat{\boldsymbol{x}}| + \frac{\hat{x}_i \hat{x}_j}{|\hat{\boldsymbol{x}}|^2},$$

where $\hat{\boldsymbol{x}} = \boldsymbol{x} - \boldsymbol{x}_0$. It may be shown that $\boldsymbol{G}$ satisfies the symmetry property

$$G_{ij}(\boldsymbol{x}, \boldsymbol{x}_0) = G_{ji}(\boldsymbol{x}_0, \boldsymbol{x}) \tag{2.7}$$

(Pozrikidis 1990*b*). The tensor $\boldsymbol{T}$ is defined as

$$T_{ijk} = -\delta_{ij} p_j + \frac{\partial G_{ij}}{\partial x_k} + \frac{\partial G_{kj}}{\partial x_i}. \tag{2.8}$$

All three of the tensors $\boldsymbol{G}$, $\boldsymbol{p}$, and $\boldsymbol{T}$ may be computed in closed form (Pozrikidis 1987); their explicit expressions are given in the Appendix.

Proceeding with the flow representation, we express the velocity field within both fluids in terms of an interfacial distribution of Green's functions

$$u_i(\boldsymbol{x}_0) = \int_{\text{Interface}} G_{ij}(\boldsymbol{x}_0, \boldsymbol{x})\, q_j(\boldsymbol{x})\, \mathrm{d}l(\boldsymbol{x}) \tag{2.9}$$

where $\boldsymbol{q}$ is the density of the distribution, and the integration is over one period of the interface, as illustrated in figure 3. Because of the properties of the Green's function, the velocity field (2.9) satisfies Stokes equation as well as the continuity

equation. In addition, it is periodic in the $x$-direction, it is continuous across the fluid interface, and it vanishes along the plane wall at $y = w$. To derive an equation for $\boldsymbol{q}$, we consider the behaviour of the surface stress across the fluid interface. The stress field corresponding to (2.9) is given by

$$\sigma_{ik,\alpha}(\boldsymbol{x}_0) = \mu_\alpha \int_{\text{Interface}} T_{ijk}(\boldsymbol{x}_0, \boldsymbol{x})\, q_j(\boldsymbol{x})\, \mathrm{d}l(\boldsymbol{x}) \tag{2.10}$$

and the surface stress on either side of the interface is given by

$$[f_i(\boldsymbol{x}_0)]_\alpha \equiv \sigma_{ik,\alpha}(\boldsymbol{x}_0)\, n_k(\boldsymbol{x}_0) = \mu_\alpha\, n_k(\boldsymbol{x}_0) \int_{\text{Interface}} T_{ijk}(\boldsymbol{x}_0, \boldsymbol{x})\, q_j(\boldsymbol{x})\, \mathrm{d}l(\boldsymbol{x}), \tag{2.11}$$

where we recall that $\alpha = 1, 2$ for the lower and the upper fluid respectively. The unit normal vector $\boldsymbol{n}$ is directed into the layer. As the interface is crossed, the integral on the right-hand side of (2.11) suffers a discontinuity (Ladyzhenskaya 1969). Introducing the Cauchy principal value integral $I$ (indicated by a PV superscript on the integral sign), equal to the mean value of the integral on either side of the interface, allows us to rewrite the surface stress on either side of the interface as

$$[f_i(\boldsymbol{x}_0)]_1 = -2\pi\mu_1\, q_i(\boldsymbol{x}_0) + \mu_1\, I_i(\boldsymbol{x}_0), \tag{2.12a}$$

$$[f_i(\boldsymbol{x}_0)]_2 = 2\pi\mu_2\, q_i(\boldsymbol{x}_0) + \mu_2\, I_i(\boldsymbol{x}_0), \tag{2.12b}$$

where

$$I_i(\boldsymbol{x}_0) \equiv n_k(\boldsymbol{x}_0) \int_{\text{Interface}}^{\text{PV}} T_{ijk}(\boldsymbol{x}_0, \boldsymbol{x})\, q_j(\boldsymbol{x})\, \mathrm{d}l(\boldsymbol{x}). \tag{2.12c}$$

Subtracting (2.12b) from (2.12a) we obtain

$$q_i(\boldsymbol{x}_0) = -\frac{1}{2\pi\mu_1(1+\lambda)}\Delta f_i(\boldsymbol{x}_0) + \frac{\beta}{2\pi}\, n_k(\boldsymbol{x}_0) \int_{\text{Interface}}^{\text{PV}} T_{ijk}(\boldsymbol{x}_0, \boldsymbol{x})\, q_j(\boldsymbol{x})\, \mathrm{d}l(\boldsymbol{x}), \tag{2.13}$$

where $\beta = (1-\lambda)/(1+\lambda)$, and $\Delta f \equiv (\boldsymbol{\sigma}_1 - \boldsymbol{\sigma}_2) \cdot \boldsymbol{n}$ is the discontinuity in the surface stress across the interface. In the particular case of gravity-driven flow, $\boldsymbol{\sigma}$ represents the modified stress tensor defined with respect to the modified pressure, $P - \rho\boldsymbol{g} \cdot \boldsymbol{x}$. Relating the discontinuity in the surface stress across the interface to the surface tension, we write

$$\Delta f = [(\rho_2 - \rho_1)\, gy + \gamma\boldsymbol{\nabla} \cdot \boldsymbol{n}]\,\boldsymbol{n}, \tag{2.14}$$

where the gravity vector points in the negative $y$-direction. Equation (2.13) is a Fredholm integral equation of the second kind for $\boldsymbol{q}$. Solving this equation allows the direct computation of the velocity or stress field by means of the fundamental representations (2.9) and (2.10). Note that when the viscosities of the two fluids are equal ($\lambda = 1$ or $\beta = 0$), the solution to (2.13) is simply $\boldsymbol{q} = -\Delta f/4\pi\mu_1$. This renders $\boldsymbol{q}$ proportional to the discontinuity in the interfacial surface stress.

Before proceeding with the solution of equation (2.13), it is imperative to examine the uniqueness of its solution. For this purpose, we investigate the existence of eigenvalues $\beta$ of the corresponding homogeneous equation

$$q_i(\boldsymbol{x}_0) = \frac{\beta}{2\pi}\, n_k(\boldsymbol{x}_0) \int_{\text{Interface}}^{\text{PV}} T_{ijk}(\boldsymbol{x}_0, \boldsymbol{x})\, q_j(\boldsymbol{x})\, \mathrm{d}l(\boldsymbol{x}). \tag{2.15}$$

Furthermore, since we are interested in developing an iterative procedure of solution, we seek to assess the convergence of the corresponding Neumann series. This requires that we consider complex as well as real eigenvalues and eigensolutions, $\beta$ and $\boldsymbol{q}$.
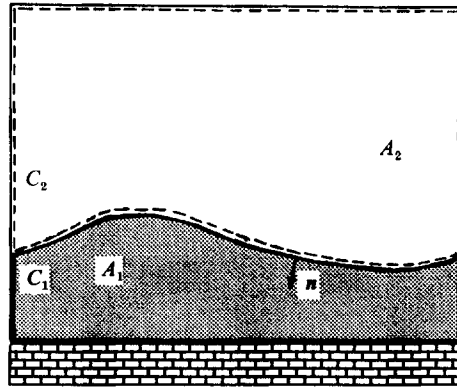
FIGURE 3. Schematic illustration of the periodically perturbed liquid layer.

Assuming that $q$ is an eigensolution to (2.15), we define the complex function

$$w_i(x_0) = \frac{1}{2\pi\mu} \int_{\text{Interface}} G_{ij}(x_0, x)\, q_j(x)\, \mathrm{d}l(x), \tag{2.16}$$

where $q$ may be complex. This represents a continuous periodic velocity field that satisfies the equations of creeping motion and vanishes along the wall. The corresponding surface stress on either side of the interface is given by

$$f^{\pm}(x_0) \equiv \sigma_{ik}^{\pm}(x_0)\, n_k(x_0) = -(\pm)\, q_i(x_0) + \frac{1}{2\pi} n_k(x_0) \int_{\text{Interface}}^{\text{PV}} T_{ijk}(x_0, x)\, q_j(x)\, \mathrm{d}l(x) \tag{2.17}$$

with a plus sign on the side of the layer, for $\alpha = 1$, and a minus sign on the side of the upper liquid, for $\alpha = 2$. Combining (2.17) with (2.15) we obtain

$$f^{\pm} = -\left(\pm 1 - \frac{1}{\beta}\right) q. \tag{2.18}$$

Next, we use the identities

$$2\mu \int_{A_1} D_{ik} D_{ik}^{*}\, \mathrm{d}A = -\int_{C_1} w_i^{*}\, \sigma_{ik}\, \hat{n}_k\, \mathrm{d}l, \tag{2.19a}$$

$$2\mu \int_{A_2} D_{ik} D_{ik}^{*}\, \mathrm{d}A = \int_{C_2} w_i^{*}\, \sigma_{ik}\, \hat{n}_k\, \mathrm{d}l, \tag{2.19b}$$

where the indicated areas and contours are depicted in figure 3. The normal vector in (2.19a) is directed inside the control area $A_1$, whereas the normal vector in (2.19b) is directed outside the control area $A_2$; $D$ and $\sigma$ are the rate of deformation tensor and the stress tensor for the flow $w$. Owing to the implicit periodicity, the contribution to the above line integrals from the straight vertical segments of $C_1$ and $C_2$ cancel each other. Also, the contribution to the line integral in (2.19a) from the wall vanishes, because $w$ vanishes along the wall. Furthermore, as the top boundary is moved to infinity, its contribution becomes negligibly small. Thus, by passing to

this limit, we find that the contour integrals in (2.19a, b) may be reduced simply to the fluid interface. Inserting (2.18) into (2.19a, b) we obtain

$$2\mu \int_{A_1} D_{ik} D_{ik}^* \, \mathrm{d}A = \left(1 - \frac{1}{\beta}\right) \int_{\text{Interface}} w_i^* q_i \, \mathrm{d}l, \qquad (2.20a)$$

$$2\mu \int_{A_2} D_{ik} D_{ik}^* \, \mathrm{d}A = \left(1 + \frac{1}{\beta}\right) \int_{\text{Interface}} w_i^* q_i \, \mathrm{d}l. \qquad (2.20b)$$

Adding these equations and noting that the integrals on the left-hand side are real and non-negative indicates that the integrals on the right-hand side are real and non-negative as well. In turn, this indicates that $\beta$ is real. Furthermore, multiplying the above equations we immediately obtain that $\beta^2 \geqslant 1$. In conclusion, (2.15) does not have real or complex eigenvalues with magnitude less than one, ensuring that (2.13) has a unique solution and that the corresponding Neumann series converges for all finite values of the viscosity ratio $\lambda$.

### 2.3. *Numerical solution of the integral equation*

Computing the evolution of the layer involves three main tasks: describing the fluid interface, solving the Fredholm integral equation, and advancing the interface in time. In our numerical procedure, we approximate the interface by a set of circular arcs defined by a set of marker points. To solve the integral equation (2.13), we use an iterative procedure similar to that developed by Pozrikidis (1990a). Our strategy is to assume an initial distribution for $q$, to compute the right-hand side of (2.13), and then to replace the originally assumed with the newly computed distribution. This procedure is guaranteed to converge, for as shown in the preceding section, the homogeneous equation (2.15) does not have any real or complex eigenvalues with magnitude less than one. The advantages of our iterative procedure over conventional matrix inversion procedures are discussed by Pozrikidis (1990a). When we have a converged value for $q$, we compute the velocity at the marker points using (2.9), and advance their position in time.

The details of our description of the fluid interface are as follows. As mentioned above, we trace a period of the interface with a set of marker points and approximate the interface by a set of circular arcs. Each arc passes through a marker point and through two other auxiliary points defined on either side of each marker point. The position of each auxiliary point is computed from the position of the four nearest marker points using Lagrange interpolation with respect to the perimeter of the polygon defined by these four marker points. The radius of curvature of the interface at each marker point, which is needed to compute the surface stress discontinuity from equation (2.14), is taken to be the radius of the corresponding arc.

The detailed tactics of our iterative solution of the integral equation are as follows. At each time we assign to each marker point a value of $q$ and approximate the $q$-distribution with a parabolic function with respect to arclength over each arc. To evaluate the double-layer integral in (2.13), we compute the value of the kernel $n_k(x_0) T_{ijk}(x_0, x)$ at eight Gauss–Legendre points over each arc, multiply them by the corresponding Gauss–Legendre weights, and store the results in a matrix. We compute the singular contribution to the principal value integral by subtracting off and integrating analytically the singularity over each arc. We then compute $q$ at the Gauss–Legendre poitns of each arc, using the above parabolic approximation, and multiply them by the previously computed values of the kernel to obtain the double-

layer integral. Applying this procedure at all marker points and using (2.13) provides us new values for $q$ at each marker point. The iterations are terminated when the magnitude of the relative difference of two successive values of both components of $q$ at every marker point differ by less than 0.0001. This procedure has the significant advantage of allowing the evaluation of the double-layer integral for different values of $q$ without requiring the costly computation of the kernel each time.

We compute the velocity of the interfacial marker points from the converged value of $q$ using (2.9). The necessary contour integration is performed in a piecewise fashion over each arc and proceeds by subtracting off and integrating analytically the logarithmic singularity over each arc. The remaining regular integration is performed using the eight-point Gauss–Legendre method. Having computed the velocities, we advance the position of the marker points using the modified Euler's method.

To minimize the number of iterations, we set the initial $q$-distribution at each time step equal to the converged value of $q$ at the previous time step. In practice, the number of iterations necessary turned out to be a strong function of the viscosity ratio. In the most extreme cases considered, $\lambda = 0.1$ and 10, ten and fifty iterations are required to solve the integral equation. We verified the accuracy of our calculations by comparing our numerical results with those predicted by linearized theory, as discussed in the next section. Furthermore, as an independent test of accuracy, we computed the area of the evolving layer. The maximum change in this area due to numerical error was less than 0.8 %.

As the interface evolves, marker points move far apart or very close to each other and regions of high curvature develop. To accommodate these features, we employ an adaptive point redistribution technique as discussed by Pozrikidis (1990 *a*). Briefly, we add a new point between two existing points if the distance between these points is greater than a specified value; we remove a point if this distance is less than a specified value. We also add a point if the angle subtended by the arc through a marker point is larger than a pre-established maximum.

With finite surface tension, we observed the onset of numerical instabilities of the sawtooth type. These are suppressed by sufficiently decreasing the size of the time step. Large surface tension requires an excessively small time step which sets pragmatic limits to our parametric investigation. A typical calculation started with 32 points and ended with 100 points. All computations were performed on the CRAY X-MP/4 computer of the San Diego Supercomputer Center. A complete calculation required approximately 10 minutes of CPU time.

## 3. Results and discussion

We study the nonlinear evolution of a liquid layer subject to an initial sinusoidal perturbation of amplitude less than 1 % of the layer thickness. As mentioned in the preceding section, the evolution is characterized by three dimensionless parameters: the viscosity ratio $\lambda$, the reduced layer thickness $\beta = kb$, and the inverse Bond number $\Gamma$. In our calculations, we fix $k$ at the value of one and choose $b$ to obtain the desired value of $\beta$. Also, we reduce distances using as characteristic lengthscale $1/k$ and time using as characteristic timescale $k\mu_1/g\Delta\rho$.

In figure 4 we present the evolution of the most unstable layer for the case of equal fluid viscosities $\lambda = 1$ and zero surface tension $\Gamma = 0$. The dashed horizontal line represents the unperturbed layer position, corresponding to a layer thickness $\beta = 1.6$. Three stages of development are apparent. At small times and up to approximately the time corresponding to the first curve, the initial disturbance
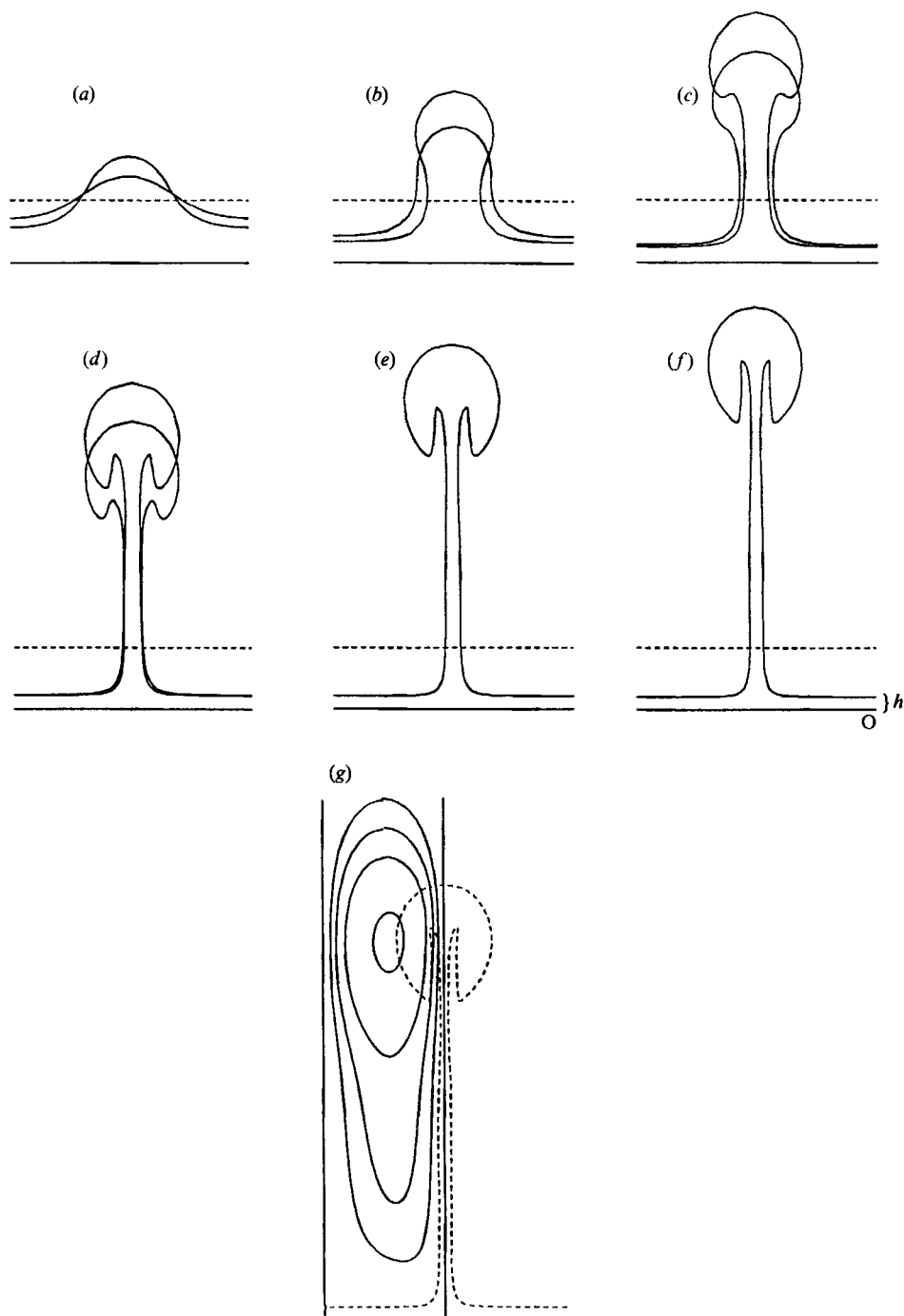
FIGURE 4. Evolution of the most unstable layer, $\beta = 1.6$, for $\lambda = 1$ and $\Gamma = 0$: (a) $t = 26$, $30$; (b) $34$, $38$; (c) $42$, $46$; (d) $50$, $54$; (e) $58$; (f) $62$; (g) instantaneous streamlines at $t = 66$.
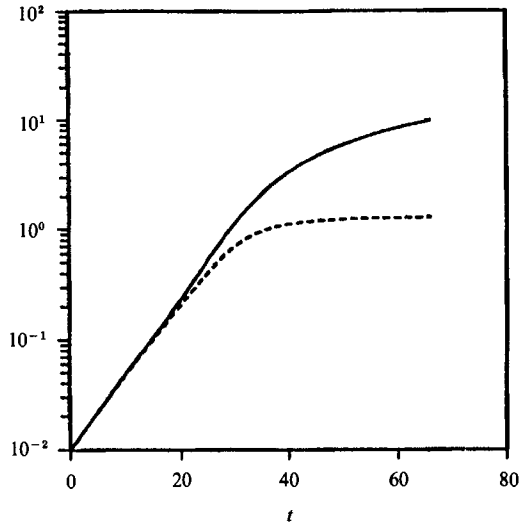
FIGURE 5. Growth of the disturbance shown in figure 4, $\lambda = 1$, $\Gamma = 0$, $\beta = 1.6$. Solid line shows maximum height above undisturbed surface. Dashed line shows maximum depth below undisturbed surface.

grows exponentially, and the layer retains its sinusoidal shape. In the second stage, a leading drop supported by a column of fluid develops, as shown in figure 4 $(a-c)$. Exterior fluid is entrained into the drop at the top of the rising column. The final stage is characterized by a slightly elongated circular drop which undergoes little change in overall shape as it rises away from the wall, figure 4 $(d-g)$. The induced fluid motion causes the supporting column to thin and the entrained exterior fluid to move deeper into the leading drop. The instantaneous streamline pattern for an advanced stage of development is shown in figure 4 $(g)$. This pattern is characterized by a family of closed streamlines, composing a viscous eddy. The centre of this eddy is approximately at the same elevation as the centre of the rising drop.

To examine the rate of the layer deformation and to compare our nonlinear results to predictions of linear theory, in figure 5 we plot the reduced height of the layer at the end and in the middle of each period with respect to time (on a semi-logarithmic scale, and wish a dashed and a solid line, respectively). During the initial growth period, we obtain straight lines with slope equal to 0.155, indicating that the disturbance grows exponentially in time. This growth rate is in perfect agreement with linear theory. Linear theory breaks down at approximately $t = 20$; past this time nonlinear effects become important, and the growth is no longer exponential. Figure 5 allows us to estimate the speed of rise of the drop formed in the advanced stages of evolution. Approximating the data represented by the solid line with a straight line, we find that past $t = 51$, the speed of rise of the drop is approximately proportional to $t^{0.71}$. Thus, the rising drop undergoes continuous acceleration as it moves away from the wall. The fact that the speed of the drop does not reach an asymptotic value but continues increasing at an algebraic rate is consistent with the ill-posed nature of the Stokes flow problem for two-dimensional, infinite flow.

We now consider a simple model for the thinning of the remnant layer left along the wall between successive rising drops. Label the point midway between rising plumes and right on the wall O, and the local thickness of the layer $h$, as indicated in figure 4 $(f)$. We expand the vertical velocity in a Taylor series about the point O,
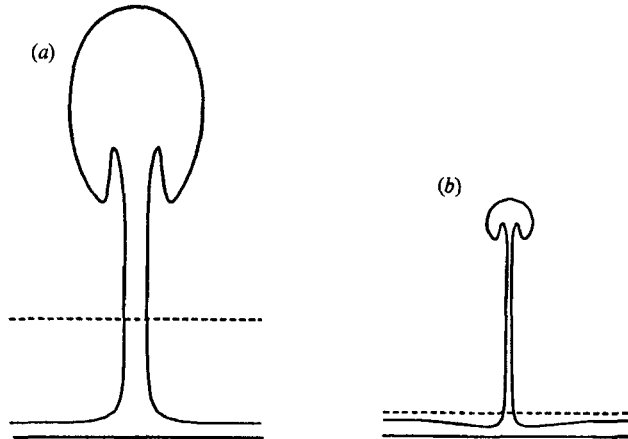
FIGURE 6. Characteristic stages in the evolution of layers thicker and thinner than the most unstable one for $\lambda = 1.0$, $\Gamma = 0$: (*a*) $\beta = 2.0$, (*b*) $\beta = 0.6$. Compare to figure 4(*d*).
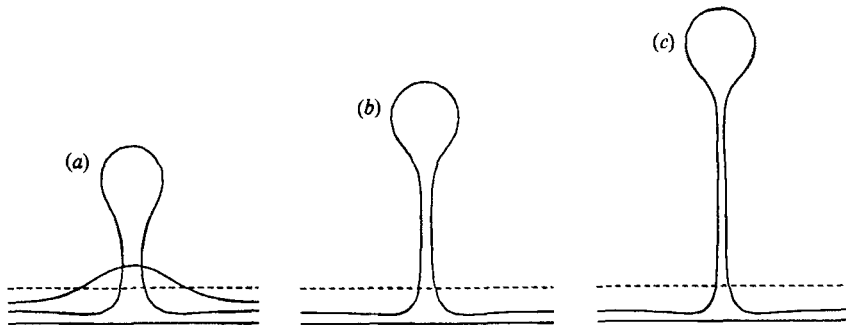
FIGURE 7. Evolution of the most unstable layer, $\beta = 0.859$, for $\lambda = 1$ and $\Gamma = 0.4$:
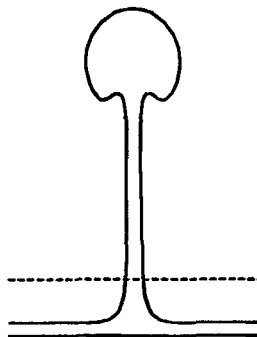(*a*) $t = 105$, $145$; (*b*) $155$; (*c*) $165.5$.

FIGURE 8. Characteristic stage in the evolution of the most unstable layer, $\beta = 1.43$, for $\lambda = 1.0$, $\Gamma = 0.5$. Compare to figures 4(*d*) and 7(*c*) to see the effect of surface tension on entrainment.

note that the zero- and first-order terms vanish because of the no-slip boundary condition and the continuity equation, respectively, and assume that the coefficient of the second-order term is nearly independent of time. In this fashion, we find $h \approx 1/(ct+d)$, where $c$ and $d$ are constants. For the case $\lambda = 1$, $\Gamma = 0$, depicted in figure 4(*a–g*), our calculated values of $c$ and $d$ are 2.45 and 1.54. The resulting model
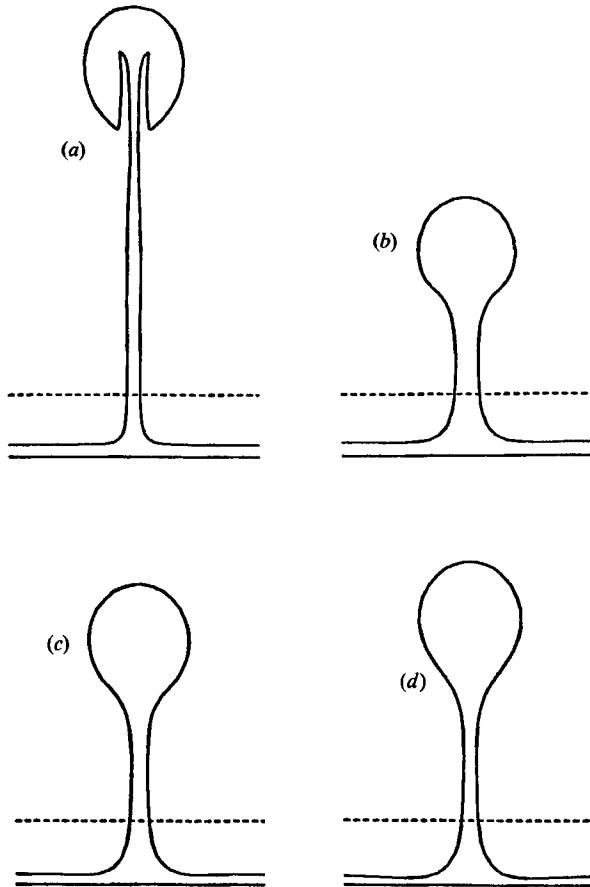
FIGURE 9. Effect of surface tension on drop formation for $\lambda = 1.0$, $\beta = 1.6$:
(a) $\Gamma = 0$, (b) 0.1, (c) 0.2, (d) 0.3.

accurately represents the thinning of the remnant layer for approximately $t > 55.0$. Physically, this implies that the remnant layer thins under the influence of the stagnation point flow generated by the rising drops, and its local dynamics are of secondary importance.

In figure 6 we illustrate the effect of initial layer thickness on the layer evolution by presenting characteristic long-time stages for layers thicker and thinner than the most unstable one. For both cases, $\lambda = 1$ and $\Gamma = 0$. We observe that asymptotically at large times, the behaviour of the layer is quite insensitive to the initial thickness of the layer. We note, however, that as the thickness of the layer increases, the size of the rising drop is also increased.

Next, we consider the effect of surface tension, maintaining $\lambda = 1$. Thus, in figure 7, we depict the evolution of the most unstable layer, $\beta = 0.859$, for $\Gamma = 0.4$. The three stages of development – exponential growth, drop formation, and drop rise – observed in the absence of surface tension exist here as well. However, at this high value of surface tension, entrainment of the exterior fluid into the drop is suppressed. For small surface tension, the drop entrains fluid as shown in figure 8 for $\Gamma = 0.05$. To illustrate the influence of surface tension on the evolution of a layer of fixed thickness, in figure 9 we present a sequence of advanced shapes for $\beta = 1.6$ and
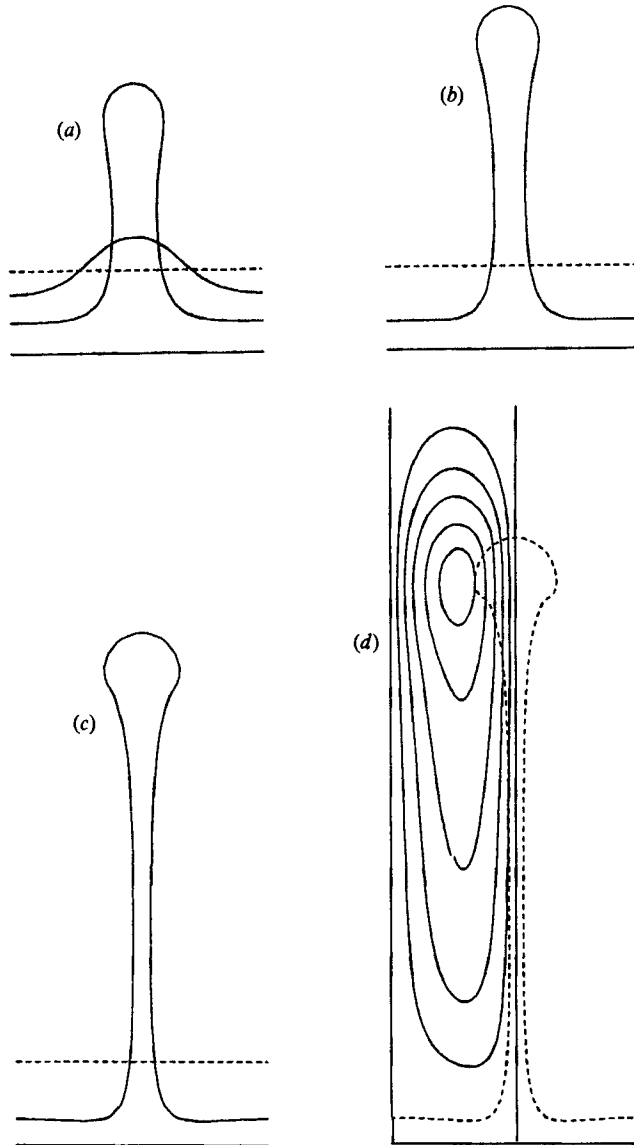
FIGURE 10. Evolution of the most unstable layer, $\beta = 2.05$, for $\lambda = 0.1$ and $\Gamma = 0$:
(a) $t = 14$, 19; (b) 20; (c) 22; (d) instantaneous streamlines at $t = 23.25$.

$\Gamma = 0, 0.1, 0.2, 0.3$. Once again, we see that entrainment disappears as surface tension is increased. The size of the drop is virtually independent of surface tension.

Having discussed the development of a liquid layer whose viscosity is the same as that of the overlying fluid, we now turn our attention to the effects of differing viscosities. We begin with a layer fluid which is ten times more viscous than the overlying fluid, $\lambda = 0.1$. Figure 10 shows the evolution of the most unstable layer in the absence of surface tension. Once again, three stages of development are apparent. The first stage, exponential growth, is identical to that of the case of equal viscosities. In the second stage, a distinct plume develops. This behaviour is in marked contrast to that observed in the second stage of evolution for $\lambda = 1$, characterized by the
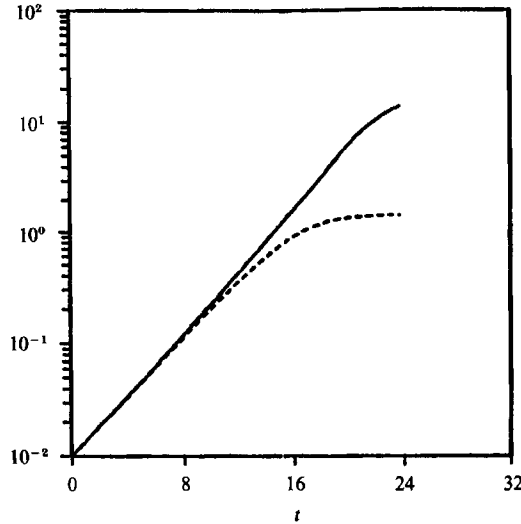
FIGURE 11. Growth of the disturbance shown in figure 10, $\lambda = 0.1$, $\Gamma = 0$, $\beta = 2.05$. Solid line shows maximum height above undisturbed surface. Dashed line shows maximum depth below undisturbed surface.

formation of a drop. The final stage is characterized by the formation of a knob of fluid on top of a rising plume. In contrast to the case $\lambda = 1$, $\Gamma = 0$, there is no entrainment of exterior fluid into the rising plume. Figure 10$(d)$ shows the instantaneous streamline pattern for an advanced stage of development. This is qualitatively similar to that shown in figure 4$(g)$ for $\lambda = 1$, $\Gamma = 0$. The growth rate of the disturbance is plotted in figure 11. The slope of the curves in the linear region is 0.3070, identical to that predicted by linear theory. At large times, the speed of rise of the knob is proportional to $t^{2.5}$. The thickness of the remnant layer decreases in time like $1/(0.0278t + 0.931)$.

To illustrate the effect of initial layer thickness for $\lambda - 0.1$, $\Gamma = 0$, in figure 12 we present characteristic advanced stages for layers thinner and thicker than the most unstable one. By comparing figure 12$(a)$ to 10$(d)$ and figure 12$(b)$ to 10$(c)$, we deduce that the asymptotic structure of the layer is quite insensitive to the initial layer thickness.

The effect of surface tension for $\lambda = 0.1$ may be deduced from figure 13 depicting the evolution of the most unstable layer for $\Gamma = 0.4$. The first and second stages of exponential growth and column formation are similar to those for $\Gamma = 0$ shown in figure 10. The final stages, however, are quite different: for $\Gamma = 0.4$, the final stage is characterized by the formation and rise of a distinct, nearly circular drop which is supported by a thinning column of fluid. Comparing figure 13$(b, c)$ with figure 7$(b, c)$ we notice that the advanced stage for $\lambda = 0.1$, $\Gamma = 0.4$ is quite similar to that for $\lambda = 1$, $\Gamma = 0.4$, even though the early stages of evolution are quite different. The advanced stage for $\lambda = 0.1$, $\Gamma = 0.05$ shown in figure 14 is composed of a rising drop and a supporting column. This structure is clearly intermediate between those for $\Gamma = 0$ and 0.4.

Moving on, we consider a layer fluid whose viscosity is one tenth that of the overlying fluid, $\lambda = 10$. As before, we first consider the evolution of the most unstable layer in the absence of surface tension, figure 15, and identify three stages of development. The first stage is exponential growth. In the second stage, a circular
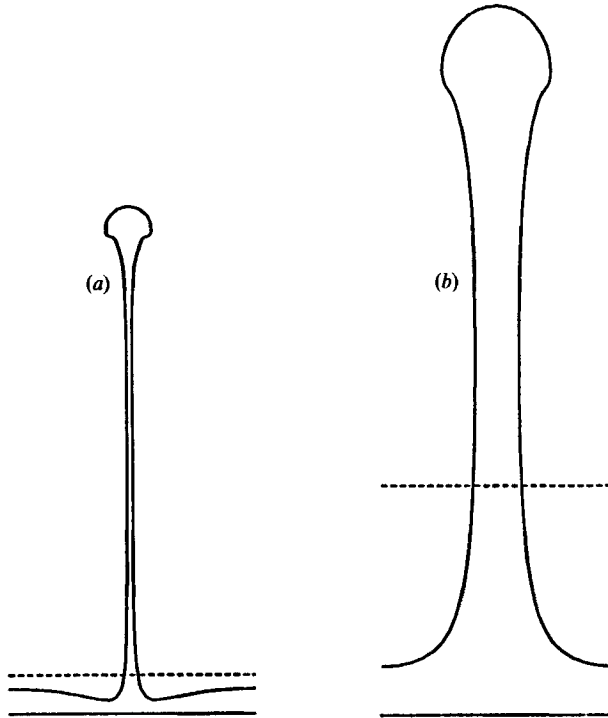
FIGURE 12. Characteristic stages in the evolution of layers thinner and thicker than the most unstable for $\lambda = 0.1$, $\Gamma = 0$: (a) $\beta = 1.0$, compare to figure 10(d); (b) $\beta = 6.0$, compare to figure 10(c).

drop is formed on top of a narrow, short stem. In the third stage, the stem is elongated and thinned, while the leading drop rises and maintains its circular shape except for a slight dimpling at the bottom. The instantaneous streamlines shown in figure 15(d) are helpful in visualizing the long-time evolution. The corresponding growth rate curves shown in figure 16 have an initial slope of 0.0294, which is identical to that predicted by linear theory. For $t > 210.0$, the speed of rise of the drop is proportional to $t^{1.03}$. For $t > 246.0$ the thickness of the remnant layer becomes proportional to $1/(0.0219t + 0.231)$. Crudely speaking, for $\lambda = 10$, the long-time structure of the layer is independent of the initial layer thickness, as illustrated in figure 17, whereas the size of the drop increases as the layer thickness is increased.

To assess the effect of surface tension for $\lambda = 10$, in figure 18 we show the evolution of the most unstable layer for $\Gamma = 0.4$. The same three stages which exist in the absence of surface tension – exponential growth, drop formation, and drop rise – are present here as well. However, at this value of surface tension, there is no dimpling of the rising drop. In the presence of only a small amount of surface tension, $\Gamma = 0.05$, slight dimpling does occur, as shown in figure 19.

We have seen that increasing surface tension at constant viscosity ratio reduces entrainment and smooths out the interface. We may also look at the same evolutions from the point of view of constant surface tension with increasing viscosity ratio. We have already noted the marked effect, shown in figures 4, 10, and 15, of differing viscosities in the absence of surface tension. The influence of viscosity ratio at $\Gamma = 0.4$ is much less dramatic; compare figures 7, 13, and 18. In all cases we see a distinct, rising, circular drop pulling a thin column of fluid. The predominant
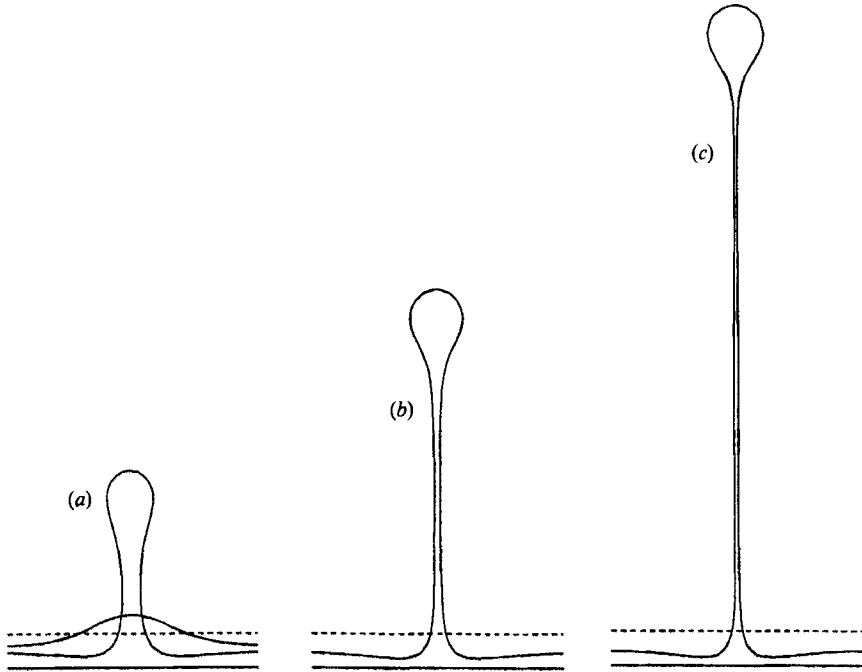
FIGURE 13. Evolution of the most unstable layer, $\beta = 0.868$, $\lambda = 0.1$ and $\Gamma = 0.4$: (a) $t = 60$, $84$; (b) $88.5$, (c) $95$.
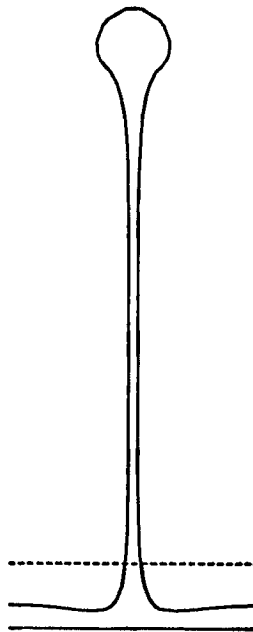


FIGURE 14. Characteristic stage in the evolution of the most unstable layer, $\beta = 1.59$, for $\lambda = 0.1$, $\Gamma = 0.05$. Compare to figure $10(c)$ and $13(c)$ to see the effect of surface tension.
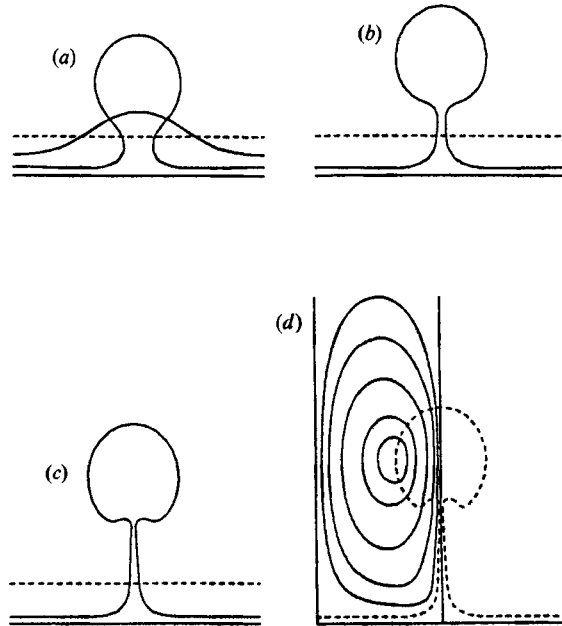
FIGURE 15. Evolution of the most unstable layer, $\beta = 0.99$, for $\lambda = 10$ and $\Gamma = 0$: (a) $t = 140$, 210; (b) 231; (c) 255; (d) instantaneous streamlines at $t = 268$.
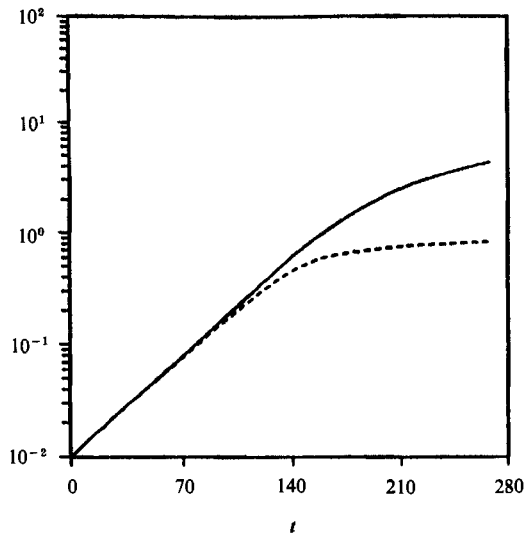


FIGURE 16. Growth of disturbance shown in figure 15, $\lambda = 10$, $\Gamma = 0$, $\beta = 0.99$. Solid line shows maximum height above undisturbed surface. Dashed line shows maximum depth below undisturbed surface.

difference is a decrease in the height above the wall at which the circular drop with a thin column first becomes evident; compare figures 13(b), 7(b), and 18(b).

We have carried out additional calculations to investigate the effect of the initial amplitude of the perturbation. Our results showed that the amplitude has a negligible influence on the overall characteristics of the evolution, although, as expected, it plays an important role in determining the timescale of the motion.
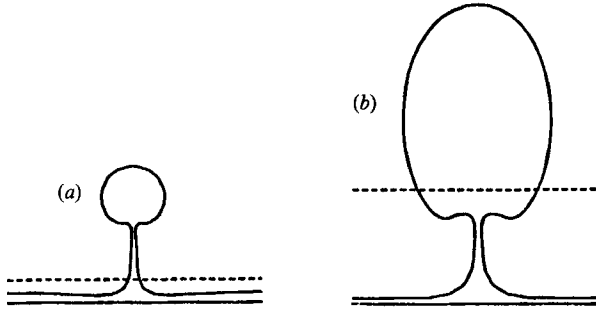
FIGURE 17. Characteristic stages in the evolution of layers thinner and thicker than the most unstable for $\lambda = 10$, $\Gamma = 0$: (a) $\beta = 0.6$, compare to figure 15 (b); (b) $\beta = 3.0$, compare to figure 15 (c).
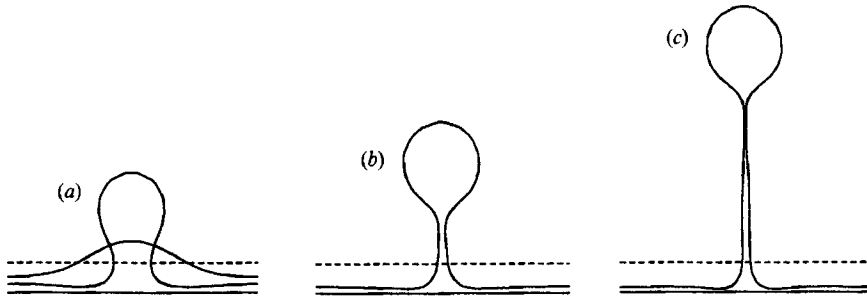


FIGURE 18. Evolution of the most unstable layer, $\beta = 0.734$, for $\lambda = 10$ and $\Gamma = 0.4$: (a) $t = 250$, 370; (b) 421.5; (c) 539.5.
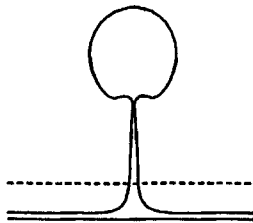


FIGURE 19. Characteristic stage in the evolution of the most unstable layer, $\beta = 0.940$, for $\lambda = 10$, $\Gamma = 0.05$. Compare to figures 15 (d) and 18 (b) to see the effect of surface tension.

Finally, we consider the development of an initial disturbance composed of two different wavelengths. In figure 20 we present the evolution of a layer of thickness $\beta = 0.80$ for $\lambda = 1.0$ and $\Gamma = 0$. The initial perturbation of the interface is two superimposed, linearly unstable sinusoidal waves with wavenumbers $k$ of 1.0 and 2.0 and zero phase shift. The shorter wave corresponds to the most unstable mode and is identical to that depicted in figure 4. For clarity of illustration, in each frame of figure 20, we draw one and a half periods of the perturbation. The same three stages of development – exponential growth, drop formation, and drop rise – present in figure 4 for a single-wavelength disturbance are seen here as well. The only difference is that the two-wave perturbation yields two different rising drops within each wavelength. These drops evolve simultaneously but at different rates. Their nonlinear interaction has only a minor influence on the qualitative features of the layer evolution.
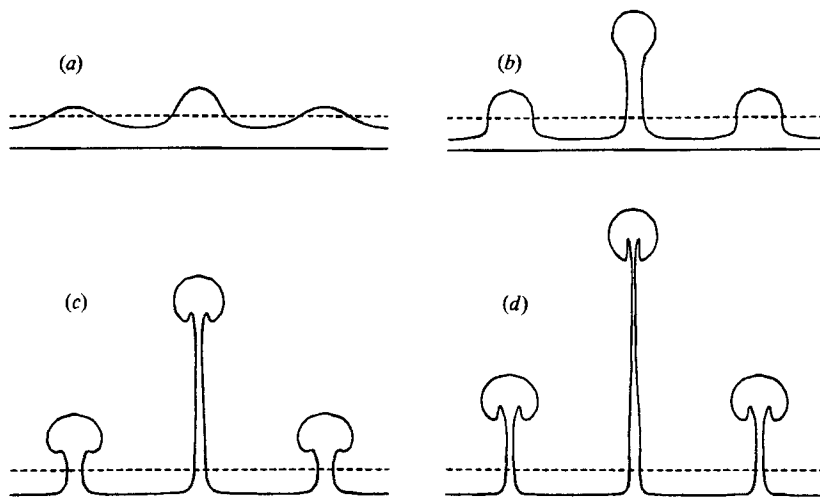
FIGURE 20. Evolution of the most unstable disturbance, $\beta = 1.6$, for $\lambda = 1$, $\Gamma = 0$ in the presence of a superharmonic disturbance $\beta = 0.8$: (a) $t = 23.6$, (b) $35.0$, (c) $44.0$, (d) $51.0$. Compare to the single-wave evolution shown in figure 4.

## 4. Concluding remarks

Under the assumption of creeping flow, we performed a parametric investigation of the Rayleigh–Taylor instability of a liquid layer resting on a plane wall below a second liquid of higher density and different viscosity. We focused our attention on cases of zero or small surface tension with our main interest the description of large layer deformations. We found that the evolution of the layer is a strong function of the viscosity ratio of the two fluids and surface tension. Specifically, we found that when the viscosity of the layer is equal to or lower than that of the overlying fluid the layer develops into an array of rising drops which are supported by thin stems of fluid. When surface tension is sufficiently small, fluid of higher density is entrained into these drops. The size of a drop is proportional to the initial layer thickness. When the layer is more viscous than the overlying fluid, the layer evolves into an array of compact rising plumes. There is no entrainment into these plumes, even at zero surface tension. This dependence on the viscosity ratio is in agreement with experimental observations pertaining to geophysical applications (Olson & Singer 1985; Whitehead 1988). At the largest value of surface tension considered, the dramatic differences due to viscosity ratio become less pronounced. While differences exist in the early stages of evolution, the final stage of evolution is rather independent of viscosity ratio; the layer reduces into an array of rising drops pulling thin columns of fluid.

Our computations show that for zero or moderate surface tension unstable layers grow without ever reaching a steady configuration. Yiantsios & Higgins (1989) performed lubrication-type calculations, as well as boundary-integral calculations (the latter for $\lambda = 1$), for the exact configuration studied in this paper. They found that for large surface tension an unstable layer may grow into a steady configuration composed of an infinite array of pendant drops. There is a critical inverse Bond number $\Gamma$ below which the layer grows without bound and above which it grows to a steady configuration. These results nicely complement our conclusions. However, the lubrication-type calculations of Yiantsios & Higgins indicated that, in the case

of suppressed motion, the viscosity of the overlying fluid plays a minor role in the layer evolution. This is in contrast with our conclusions for large deformations.

Our analysis assumes Stokes flow throughout the entire layer evolution. We find that for zero or moderate surface tension the speed at which a drop or plume rises increases algebraically with time. This means that eventually the velocities in the flow will become large enough to invalidate the Stokes flow assumption. The point in the evolution at which this happens depends on the specific fluids being considered. Our analysis also assumes that two-dimensional flow is maintained. In reality, small deviations from two-dimensionality will grow in time and the developing structures will become three-dimensional. Thus, the rising cylindrical plumes will transform into spherical drops. The behaviour of these drops as they rise away from the solid wall was recently investigated by Pozrikidis (1990b), and the reader is referred to his paper for further details.

## Appendix. The periodic Green's function for two-dimensional flow bounded by a plane wall

First, we consider the flow induced by an array of two-dimensional Stokeslets located at $x_n = (x_n, y_n)$, where $n$ runs between $-N$ and $N$, and $x_n = x_0 + nl$, $y_n = y_0$. The corresponding Green's function may be conveniently derived by summing the flows produced by the individual Stokeslets. We thus write for the velocity tensor $\boldsymbol{G}$

$$G_{ij}(x, x_0) = \sum_{n=-N}^{n=N} \left[ -\delta_{ij} \ln (r_n) + \frac{\hat{x}_{n,i} \hat{x}_{n,j}}{r_n^2} \right], \tag{A 1}$$

where $\hat{x} = x - x_n$, $r_n = |\hat{x}_n|$. All lengths have been reduced using the wavenumber $k = 2\pi/l$. To obtain the periodic Green's function, we let $N$ go to infinity. Since the sum in (A 1) diverges, it is imperative to discard the infinite constant contribution. Using the regularized formula

$$A \equiv \sum_{n=-\infty}^{\infty} \ln (r_n) = \ln [\cosh (\hat{y}_0) - \cos (\hat{x}_0)]^{\frac{1}{2}} + \ln 2 \tag{A 2}$$

(Lamb 1932, p. 71) and differentiating, we obtain

$$\sum_{n=-\infty}^{\infty} \frac{\hat{x}_n}{r_n^2} = \frac{\partial A}{\partial \hat{x}_0} \equiv A_x, \quad \hat{y}_0 \sum_{n=-\infty}^{\infty} \frac{1}{r_n^2} = \frac{\partial A}{\partial \hat{y}_0} \equiv A_y. \tag{A 3a, b}$$

Considering (A 1), passing to the limit as $N$ goes to infinity, and using (A 2) and (A 3) we obtain the four components of the Green's function periodic velocity tensor

$$\boldsymbol{G}^{\mathrm{P}} = \begin{bmatrix} -A - \hat{y}_0 A_y + 1 & \hat{y}_0 A_x \\ \hat{y}_0 A_x & -A + \hat{y}_0 A_y \end{bmatrix}. \tag{A 4}$$

The superscript P stands for periodic. The corresponding pressure vector $\boldsymbol{p}$ is given by

$$\boldsymbol{p}^{\mathrm{P}} = 2\begin{bmatrix} A_x \\ A_y \end{bmatrix}, \tag{A 5}$$

whereas the stress tensor is given by

$$\begin{bmatrix} T^{\mathrm{P}}_{xxx} & T^{\mathrm{P}}_{xxy} \\ T^{\mathrm{P}}_{yxx} = T^{\mathrm{P}}_{xyx} & T^{\mathrm{P}}_{yxy} = T^{\mathrm{P}}_{xyy} \\ T^{\mathrm{P}}_{yyx} & T^{\mathrm{P}}_{yyy} \end{bmatrix} = 2\begin{bmatrix} \boldsymbol{\nabla}\cdot(-A, -\hat{y}_0 A_y) & \boldsymbol{\nabla}\cdot(\hat{y}_0 A_x, -A) \\ \boldsymbol{\nabla}\cdot(\hat{y}_0 A_x, -A) & \boldsymbol{\nabla}\cdot(-A, \hat{y}_0 A_x) \\ \boldsymbol{\nabla}\cdot(-A, \hat{y}_0 A_x) & \boldsymbol{\nabla}\cdot(-\hat{y}_0 A_x, -A) \end{bmatrix}. \tag{A 6}$$

All indicated differentiations are with respect to $\hat{\boldsymbol{x}}_0$.

The Green's function for a flow which is periodic in the $x$-direction and has zero velocity on a wall located at $y = w$ is derived in a similar manner, by summing the fundamental solution for zero velocity on a plane (see Blake 1971)

$$\boldsymbol{G}^{\mathrm{WP}} = \boldsymbol{G}^{\mathrm{P}}(\tilde{x}) - \boldsymbol{G}^{\mathrm{P}}(\tilde{x}) + 2h^2\boldsymbol{G}^{\mathrm{PDP}}(\tilde{x}) - 2h\boldsymbol{G}^{\mathrm{SDP}}(\tilde{x}), \tag{A 7}$$

where $h = y_0 - w$, $\tilde{x} = x - x_0^{\mathrm{IM}} =$, $x_0^{\mathrm{IM}} = (x_0, 2w - y_0)$. The superscripts possess the following meanings: WP means wall, periodic; SDP means Stokes doublet, periodic; and PDP means potential doublet, periodic. The tensor $\boldsymbol{G}^{\mathrm{PDP}}$ is given by

$$G^{\mathrm{PDP}}_{ij}(\hat{x}) = \sum_{n=-\infty}^{\infty} \pm\frac{\partial}{\partial\hat{x}_{n,j}}\left(\frac{\hat{x}_{n,i}}{r_n^2}\right) \tag{A 8a}$$

with a plus sign for $j = 1$ for the $x$-axis, and minus sign for $j = 2$ for the $y$-axis. We find

$$\boldsymbol{G}^{\mathrm{PDP}}(\hat{x}) = \begin{bmatrix} A_{yy} & A_{xy} \\ -A_{xy} & A_{yy} \end{bmatrix}. \tag{A 8b}$$

The tensor $\boldsymbol{G}^{\mathrm{SDP}}$ is given by

$$G^{\mathrm{SDP}}_{ij}(\hat{x}) = \pm\frac{\partial G^{\mathrm{P}}_{iy}}{\partial\hat{x}_j}. \tag{A 9a}$$

We find

$$\boldsymbol{G}^{\mathrm{SDP}}(\hat{x}) = \begin{bmatrix} -\hat{y}_0 A_{yy} & -A_x - \hat{y}_0 A_{xy} \\ -A_x + \hat{y}_0 A_{xy} & -\hat{y}_0 A_{yy} \end{bmatrix}. \tag{A 9b}$$

The pressure vector corresponding to the periodic Green's function is given by

$$\boldsymbol{p}^{\mathrm{WP}} = \boldsymbol{p}^{\mathrm{P}}(\tilde{x}) - \boldsymbol{p}^{\mathrm{P}}(\tilde{x}) - 2h\boldsymbol{p}^{\mathrm{SDP}}(\tilde{x}), \tag{A 10}$$

where

$$\boldsymbol{p}^{\mathrm{SDP}} = 2\begin{bmatrix} A_{xy} \\ -A_{yy} \end{bmatrix}. \tag{A 11}$$

Finally, the stress tensor is given by

$$\boldsymbol{T}^{\mathrm{WP}} = \boldsymbol{T}^{\mathrm{SP}}(\hat{x}) - \boldsymbol{T}^{\mathrm{SP}}(\tilde{x}) + 2h^2\boldsymbol{T}^{\mathrm{PDP}}(\tilde{x}) - 2h\boldsymbol{T}^{\mathrm{SDP}}(\tilde{x}). \tag{A 12}$$

The tensors $\boldsymbol{T}^{\mathrm{SDP}}$ and $\boldsymbol{T}^{\mathrm{DP}}$ may be computed by straightforward differentiation using

$$T^{\mathrm{PDP}}_{ijk} = \frac{\partial G^{\mathrm{PDP}}_{ij}}{\partial x_k} + \frac{\partial G^{\mathrm{PDP}}_{kj}}{\partial x_i} \tag{A 13}$$

$$T^{\mathrm{SDP}}_{ijk} = -\delta_{ik}p^{\mathrm{SDP}}_j + \frac{\partial G^{\mathrm{SDP}}_{ij}}{\partial x_k} + \frac{\partial G^{\mathrm{SDP}}_{kj}}{\partial x_i}. \tag{A 14}$$

These forms are convenient for computer programming.

## REFERENCES

BABCHIN, A. J., FRENKEL, A. L., LEVICH, B. G. & SIVASHINSKY, G. I. 1983 Nonlinear saturation of Rayleigh–Taylor instability in thin films. *Phys. Fluids* **26**, 3159–3161.

BAKER, G. R., McCRORY, R. L., VERDON, C. P. & ORSAG, S. A. 1987 Rayleigh–Taylor instability of fluid layers. *J. Fluid Mech.* **178**, 161–175.

BLAKE, J. R. 1971 A note on the image system for a stokeslet in a no-slip boundary. *Proc. Camb. Phil. Soc.* **70**, 303–310.

CHANDRASEKHAR, S. 1961 *Hydrodynamic and Hydromagnetic Stability*. Dover.

GARDNER, C. L., GLIMM, J., McBRYAN, O., MENIKOFF, R., SHARP, D. H. & ZHANG, Q. 1988 The dynamics of bubble growth for Rayleigh–Taylor unstable interfaces. *Phys. Fluids* **31**, 447–465.

HOOPER, A. P. & BOYD, W. G. 1983 Shear-flow instability at the interface between two viscous fluids. *J. Fluid Mech.* **128**, 507–528.

JACOBS, J. W. & CATTON, I. 1988a Three-dimensional Rayleigh–Taylor instability. Part 1. Weakly nonlinear theory. *J. Fluid Mech.* **187**, 329–352.

JACOBS, J. W. & CATTON, I. 1988b Three-dimensional Rayleigh–Taylor instability. Part 2. Experiment. *J. Fluid Mech.* **187**, 353–371.

JAIN, R. K. & RUCKENSTEIN, E. 1976 Stability of stagnant films on a solid surface. *J. Colloid Interface Sci.* **54**, 108–116.

KERR, R. 1988 Simulation of Rayleigh–Taylor flows using vortex blobs. *J. Comput. Phys.* **76**, 48–84.

KEUNINGS, R. & BOUSFIELD, D. W. 1987 Analysis of surface tension driven leveling in viscoelastic films. *J. Non-Newtonian Fluid Mech.* **22**, 219–233.

LADYZHENSKAYA, O. A. 1969 *The Mathematical Theory of Viscous Incompressible Flow*. Gordon & Breach.

LAMB, H. 1932 *Hydrodynamics*, 6th edn. Cambridge University Press.

MENIKOFF, R., MJOLSNESS, R. C., SHARP, D. H. & ZEMACH, C. 1977 Unstable normal mode for Rayleigh–Taylor instability in viscous fluids. *Phys. Fluids* **20**, 2000–2004.

MENIKOFF, R., MJOLSNESS, R. C., SHARP, D. H. & ZEMACH, C. 1978 Initial value problem for Rayleigh–Taylor instability of viscous fluids. *Phys. Fluids* **21**, 1674–1687.

OLSON, P. & SINGER, H. 1985 Creeping plumes. *J. Fluid Mech.* **158**, 511–531.

ORCHARD, S. E. 1963 On surface levelling in viscous liquids and gels. *Appl. Sci. Res.* **A11**, 451.

POZRIKIDIS, C. 1987 Stokes flow in two-dimensional channels. *J. Fluid Mech.* **180**, 495–514.

POZRIKIDIS, C. 1990a The instability of a moving viscous drop. *J. Fluid Mech.* **210**, 1–21.

POZRIKIDIS, C. 1990b The deformation of a viscous drop moving normal to a plane wall. *J. Fluid Mech.* **215**, 331–363.

RAYLEIGH, LORD 1900 *Scientific Papers*, vol. II. Cambridge University Press.

SHARP, D. H. 1984 An overview of Rayleigh–Taylor instability. *Physica* **12D**, 3–18.

TRYGGVASON, G. 1988 Numerical simulations of the Rayleigh–Taylor instability. *J. Comput. Phys.* **75**, 253–282.

VERDON, C. P., McCRORY, R. L., MORSE, R. L., BAKER, G. R., MEIRON, D. I. & ORSZAG, S. A. 1982 Nonlinear effects of multifrequency hydrodynamic instabilities on ablatively accelerated thin cells. *Phys. Fluids* **25**, 1653–1674.

WHITEHEAD, J. A. 1988 Fluid models of geological hotspots. *Ann. Rev. Fluid Mech.* **20**, 61–87.

YIANTSIOS, S. G. & HIGGINS, B. G. 1989 Rayleigh–Taylor instability in thin viscous films. *Phys. Fluids* A **1**, 1484–1501.

ZUFIRIA, J. A. 1988 Bubble competition in Rayleigh–Taylor instability. *Phys. Fluids.* **31**, 440–446.